OMAE2022-78288

WAKE INTERACTION BETWEEN TWO FLOATING OFFSHORE WIND TURBINES WITH BLADE DEFORMATION

Yang Huang
Department of Naval Architecture, Ocean and Marine Engineering, University of Strathclyde, Glasgow, UK

Qing Xiao
Department of Naval Architecture, Ocean and Marine Engineering, University of Strathclyde, Glasgow, UK
*Corresponding author: qing.xiao@strath.ac.uk

Decheng Wan
Computational Marine Hydrodynamic Lab (CMHL), School of Naval Architecture, Ocean and Civil Engineering, Shanghai Jiao Tong University, Shanghai, China

ABSTRACT

With the increasing size and flexibility of wind turbine blades, the impacts of blade deformation on the aerodynamic performance of wind turbines are becoming more and more important. To better understand the influence of blade flexibility on the wake interaction of FOWTs, a coupled analysis tool composed of an improved ALM and in-house CFD code based on OpenFOAM is employed to perform numerical simulations for two spar-type FOWTs with a tandem layout under given regular wave and uniform wind conditions. Coupled aero-hydro-elastic responses of the floating wind turbine are compared for rigid blades and flexible blades scenarios to examine the impacts of blade deformation on the wake interaction. The variations of aerodynamic loads, wake characteristics, and floating platform dynamics motions' responses are fully examined. Our results show that the blade deformation of downstream FOWT is smaller than that of upstream FOWT due to the turbine wake. The time-mean aerodynamic load coefficients of both upstream and downstream FOWT decrease due to the shape deformation of the blade. Moreover, the wake vortexes are found to be more stable when the blade is flexible.

Keywords: FOWT, Improved ALM, Blade deformation, Aero-hydro-elastic responses, Wake characteristics, CFD.

1. INTRODUCTION

With the rapid development of the offshore wind industry, the technology of offshore wind turbines is advancing towards the direction of large-scale, deep-sea areas and clustering [1]. The Floating Offshore Wind Turbines (FOWTs) have gradually evolved from conceptual designs to actual engineering applications. Limited by the layout space and manufacturing cost, the negative wake interaction in an offshore wind farm is inevitable, and has a negative impact on the inflow conditions to the downstream wind turbines, thereby reducing the turbine power generation and increasing the structure fatigue loading [2]. Moreover, with the gradual increase in the size of wind turbines, the phenomenon of structural deformation of aero-elastic blade is becoming more profound. Due to the coupling between wind turbine aerodynamics and floating platform hydrodynamics, wake interaction will further influence the dynamic motion response of the FOWT. A better understanding on the wake interaction of FOWTs through considering the aeroelasticity of wind turbine blade is therefore necessary.

Wake interaction phenomena for the onshore wind farm have been investigated in previous studies. For instance, Troldborg et al. [3] analyzed the wake interaction of two wind turbines under different inflow conditions using the flow solver EllipSys3D [4] and Actuator Line Model (ALM). Their results showed that the combined effect of inflow shear and wake rotation led to the rotationally asymmetric development of the wake and further resulted in an inhomogeneous distribution of the aerodynamic blade loads on the downstream turbine. Ambient turbulence would speed up the recovery of upstream wake deficit and hence increase the average blade loads of downstream wind turbine. Chanprasert et al. [5] modelled wake interactions in a wind turbine array using an open-source code SOWFA [6] and Large-Eddy Simulation (LES). The influence of atmospheric stability and turbine yaw condition on the development of wake characteristics was discussed. Compared with the fixed yaw turbine condition, the downstream wind turbine with a baseline active yaw controller experienced higher fatigue loading under Atmospheric Boundary Layer (ABL) flow. Based on the actuator line technique and LES, Nilsson et al. [2] and Rai et al. [7] modelled the wake development of the well-known Lillgrund wind farm composed of forty-eight 2.3-MW wind turbines. Their results indicated that a higher inflow

turbulence intensity led to slightly increase of total power output of the wind farm.

The above studies are focused on onshore wind farm, while investigation on offshore floating wind farm is rarely covered. This is due to the complexity of a FOWT system and its expensive computational modelling cost. Attempts were made by Rezaeiha and Micallef [8, 9] where in their studies, Computational Fluid Dynamic (CFD) method and Actuator Disk Model (ADM) were utilized to model two tandem FOWTs. A prescribed surge motion was imposed on the upstream FOWT, while downstream FOWT was fixed. The surge motion of upstream rotor was found to increase the aerodynamic power of both FOWTs, and it also enhanced the wake fixing and further led to a faster wake deficit recovery of downstream FOWT. It is also noted that studies on the wake interactions of FOWTs with six-degree-of-freedom (6DoF) motions are very limited. Huang et al. [10, 11] studied the wake interactions of two spar-type FOWTs with 6DoF motions using a fully coupled aero-hydrodynamic numerical modelling tool [12]. An Unsteady Actuator Line Model (UALM) [13] was used to model the aerodynamics of wind turbine. According to their results, the downstream FOWT experienced lower average aerodynamic loads and fluctuation amplitude than the upstream FOWT.

Large-scale offshore wind turbine blades have an innate aeroelasticity due to their structural nature. Analysis for such FOWTs has to be performed using a coupled aero-hydrodynamic model considering the potential blade deformation. Several software have been developed to perform the coupled aero-hydro-elastic simulation at different levels. One category is the reduced-order tools such as OpenFAST [14] and HAWC2 [15]. In these tools, the Blade-Element-Momentum (BEM), Free-wake Vortex Method (FVM), and potential flow theory are utilized to predict the aerodynamic loading and the hydrodynamic responses, specifically. Compared to a higher-order and fidelity CFD modelling, these tools excel in terms of fast computation, thus favored by many researchers. For example, Bae and Kim [16] investigated the coupled aero-hydro-elastic responses of a FOWT considering wind, wave, and they are currently using OpenFAST for both operational and survival sea conditions. It should be noted that although these simplified models can predict the aerodynamic loading, platform motion and blade deformation, the wind field around the FOWT cannot be captured. To better understand the flow details and wake structure, the higher-order CFD method can be employed as one option. Liu et al. [17] developed a coupled analysis tool based on OpenFOAM and multi-body dynamics tool. The code was used to study the impact of blade aeroelasticity on the aerodynamic loading with a prescribed surge motion imposed on the platform. The study was also extended to the identification on the wake field characteristics, which is caused by the blade structural deformation. Even though there are existing studies on the aeroelasticity of wind turbine blade, the impact of aeroelasticity on the wake interaction in a floating offshore wind farm is a novel investigation.

In this study, a spar-type floating wind turbine composed of the NREL 5-MW wind turbine and the OC3-Hywind Spar platform is investigated. Numerical simulations are performed for two FOWTs in a tandem arrangement at a given regular wave and uniform wind condition. The 6DoF platform motions of FOWTs are considered. Coupled wind-wave dynamic responses of the FOWTs are compared with rigid and flexible blade scenarios to examine the impacts of blade deformation on the wake interaction. The variations of aerodynamic loading, the wake characteristics, and the platform motion responses, as a result of blade deformation, are fully examined.

2. NUMERICAL METHODS

2.1 Aero-hydro-elastic modelling

To tackle this aero-hydro-elastic modelling problem, an in-house CFD method [12] based on an open-source toolbox OpenFOAM is deployed, and validation for this coupled analysis tool has been done in the previous publications [12, 18, 19]. To reduce the computational cost, an improved ALM is employed instead of blade-resolved method for the analysis of unsteady wind turbine aerodynamics. The structural deformation of the turbine blade is dealt with using the Euler-Bernoulli beam model and one-dimensional (1D) Finite Element Method (FEM) method [20]. The CFD method and Piecewise Extrapolation Method (PEM) are used to predict the hydrodynamic responses of floating support platform with a mooring system. The above approaches take the coupling between the blade deformation, the aerodynamic load, and the platform motion response into consideration.

The original ALM was developed for fixed wind turbines and unable to deal with a FOWT with flexible blades. To apply ALM to a FOWT with elastic blades, the original ALM method is modified, named an Improved ALM. Figure 1 illustrates a schematic diagram of the problem to be studied, in particular, the coordinate systems and speed vectors at the blade section. The velocity induced by both platform motion and blade deformation are included, thus the unsteady aerodynamics of FOWT can be predicted. As can be seen in Eq. (1), the relative wind speed U_{rel} experienced by the blade is composed of four parts: inflow wind speed U_{in}, rotational speed Ωr, additional velocity U_{M} induced by platform motion, and additional velocity U_{S} induced by blade deformation.

$$U_{\text{rel}} = U_{\text{in}} + \Omega r + U_{\text{M}} + U_{\text{S}} \qquad (1)$$

where Ω is the rotational speed, r represents the rotational radius of the blade section. U_{in} is obtained by interpolating based on the flow velocity at the grid nodes near the actuator point. U_{rel} is then projected into the blade-aligned coordinate system to get the inflow angle φ. Then Angle of Attack (AoA) α is obtained.

$$\alpha = \varphi - \theta_{\text{twist}} - \theta_{\text{pitch}} - \theta_{\text{torsion}} \qquad (2)$$

$$\varphi = \arctan(U_0/U_1) \qquad (3)$$

where θ_{twist}, θ_{pitch} and θ_{torsion} give the local twist angle, the blade pitch angle, and the torsional angle induced by blade torsional deformation, respectively. U_0 and U_1 are the projection components of U_{rel} along x_2 and y_2 directions, respectively. According to α and a two-dimensional airfoil database obtained from experiment data or numerical simulation, the aerodynamic

load acting on the blade section can be obtained. To reproduce the turbine wake, the aerodynamic forces are further projected into the flow field using a regularization function [21].

$$\eta_\varepsilon(d) = \frac{1}{\varepsilon^3 \pi^{3/2}} exp\left[-\left(\frac{d}{\varepsilon}\right)^2\right] \tag{4}$$

where d represents the distance from the grid node to the blade section. ε is a constant parameter, which is used to regulate the projection strength of aerodynamic force. The projected body forces representing the wind turbine blades are added into the momentum equations.
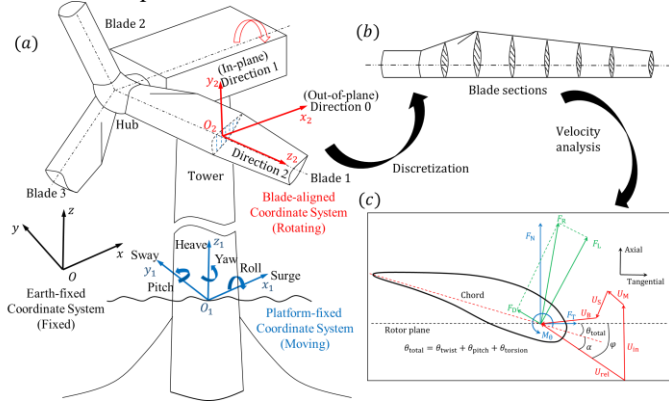
FIGURE 1: SCHEMATIC DIAGRAM OF IMPROVED ALM

Schematical diagram of blade deformation is shown in Figure 2. In structural model, the wind turbine blade is discretized into a series of beam elements, and the shape of blade element is defined by Hermite function. Each beam element has two nodes, and each node allows the bending deformation along flap-wise direction δ_0, along edge-wise direction δ_1, and the torsional deformation δ_θ. Based on the shape function and D'Alembert's principle, element stiffness and mass matrixes can be developed, including the bending stiffness matrix and torsional stiffness matrix. Then global stiffness and mass matrixes are obtained by assembling the element matrixes. The total external forces lead to the deformation of blades. These forces include the gravity forces, the aerodynamic forces and the centrifugal forces. Refer to Chen's study for more details about the structural model [20].
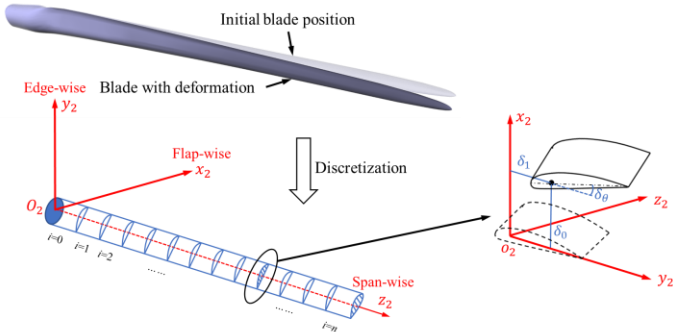

FIGURE 2: SCHEMATIC DIAGRAM OF BLADE STRUCTURAL DEFORMATION

Hydrodynamic modelling of the floating support platform is achieved by CFD method. By integrating the pressure on platform surface, hydrodynamic forces acting on platform are obtained. The 6DoF motion equations are then solved to predict the motion response of the FOWT under the combined effect of hydrodynamic, aerodynamic and mooring forces. The flow modelling is achieved using in-house CFD code based on OpenFOAM modifications. Volume of Fluid (VoF) method with bounded compression technique is selected as a method to capture the wave-wind free-surface, and PEM is used to calculate the mooring tension. It is worth mentioning that since there is no solid blades while using an improved ALM, the simulation of blade boundary layer is not required. In the ALM method, the blades are modelled as compact force lines added in the form of body forces to the momentum equation of the flow solver. Therefore, the complicated techniques used to deal with the dynamic motion of CFD mesh, such as sliding mesh and overset grid, are not required. The deformed grid technique is capable of handling the motions involved in the simulation of FOWT. A two-way coupling approach is employed to account for the interaction of aerodynamics, hydrodynamics, and blade deformation.

2.2 Governing equations

To describe the two-phase flow around the FOWT, 3D Reynolds-Averaged Navier-Stokes (RANS) equations with k-ω SST turbulence model are chosen as the governing equations.

$$\nabla \cdot \mathbf{U} = 0 \tag{5}$$

$$\frac{\partial(\rho\mathbf{U})}{\partial t} + \nabla \cdot \left(\rho(\mathbf{U} - \mathbf{U}_g)\right)\mathbf{U} = -\nabla p_d - \mathbf{g} \cdot x\nabla\rho + \nabla \cdot (\mu_{eff}\nabla\mathbf{U})$$
$$+ (\nabla\mathbf{U}) \cdot \nabla\mu_{eff} + \boldsymbol{f}_\sigma + \boldsymbol{f}_s + \boldsymbol{f}_\varepsilon \tag{6}$$

where $\mathbf{U}$ and $\mathbf{U}_g$ are the flow velocity and CFD grid velocity, respectively. ρ represents the mixture density of air phase and water phase. p_d is the dynamic pressure. $\mathbf{g}$ is the gravity acceleration vector. μ_{eff} is the effective dynamic viscosity. $\boldsymbol{f}_\sigma$ is the surface tension term. $\boldsymbol{f}_\sigma$ is the source term in sponge layer, which is set to absorb the wave reflection. $\boldsymbol{f}_\varepsilon$ represents the body forces acting on the wind turbine blades.

Governing equations for the structural analysis are presented as equations (7~8), which are solved by Newmark-beta approach [22].

$$[\mathbf{M}]\ddot{\boldsymbol{y}} + [\mathbf{C}]\dot{\boldsymbol{y}} + [\mathbf{K}]\boldsymbol{y} = \boldsymbol{F}(t) \tag{7}$$

where $\mathbf{M}$, $\mathbf{C}$ and $\mathbf{K}$ are the mass, damping, and stiffness matrixes, respectively. $\boldsymbol{F}$ is the external forces leading to the blade deformation, which vary with time. As mentioned above, $\mathbf{M}$ and $\mathbf{K}$ are derived based on Hermite shape function and D'Alembert's. Moreover, $\mathbf{C}$ can be generated by $\mathbf{M}$ and $\mathbf{K}$ [23~25].

$$[\mathbf{C}] = a_1[\mathbf{M}] + a_2[\mathbf{K}] \tag{8}$$

where a_1 and a_2 are coefficients determined by the damping ratio and the natural frequency of the wind turbine blade.

3. SIMULATION SET UP

3.1 FOWT model

A spar-type FOWT, integrating of the NREL 5-MW wind turbine and the OC3-Hywind Spar platform, is modelled, as

shown in Figure 3. The NREL 5-MW wind turbine is a typical three-blade offshore wind turbine with a rotor diameter of 126m and a hub height of 90m. The rated wind speed and corresponding rotor speed of the wind turbine are 11.4m/s and 12.1rpm respectively. The OC3-Hywind spar platform is composed of two cylinders with different diameters and a circular truncated table in the middle. The draft of platform is as deep as 120m. The motion of floating support platform is constrained by using catenary lines evenly distributed around the platform with a radius of 853.87m. The main parameters of this FOWT are indicated in Figure 3, and more detailed information can be found in the references [26, 27].

(a) FOWT MODEL   (b) MOORING SYSTEM
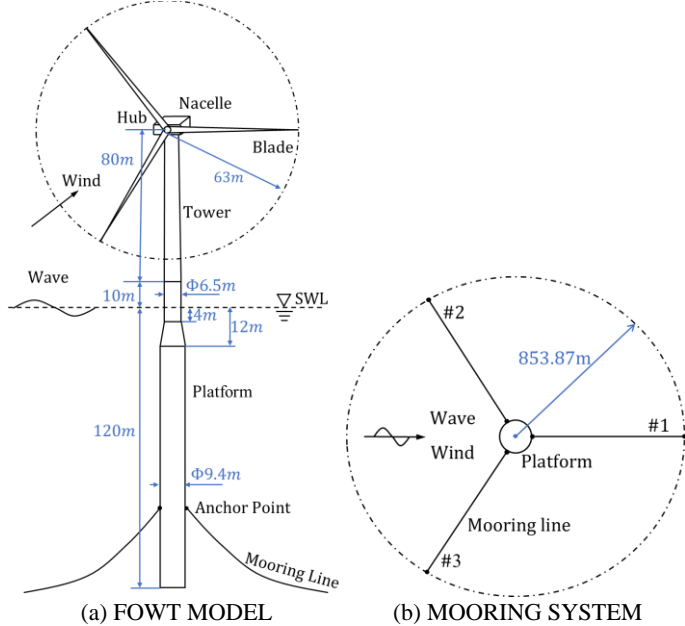
FIGURE 3: SCHEMATIC DIAGRAM OF OC3-HYWIND SPAR FOWT

3.2 Computational domain
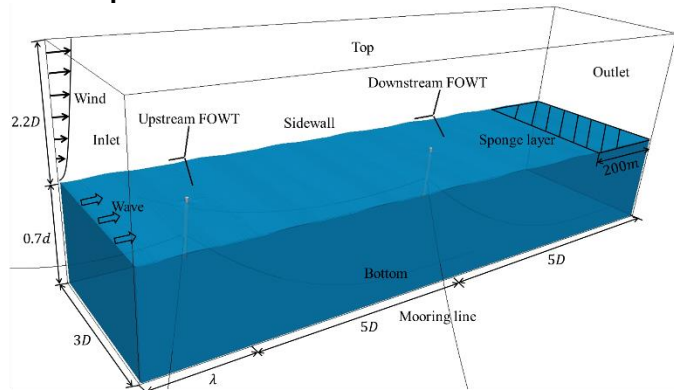
FIGURE 4: COMPUTATION DOMAIN LAYOUT

A cuboid region is generated as the computational domain for the numerical simulation. As shown in Figure 4, two FOWTs are both located in the mid-longitudinal plane of the computational domain. The distance between two FOWTs is $5D$ (D=126m is the rotor diameter). The distance from the upstream FOWT (WT #1) to the inlet boundary is λ (λ is the wavelength). The downstream FOWT (WT #2) is located $5D$ away from the outlet boundary. The width of computational domain is $3D$. The depth of water phase is set to $0.7d$ (d=320m is the operational water depth). Considering the expansion of turbine wake, the air phase has a height of $2.2D$, a sponge layer with a length of 200m is placed before the outlet boundary to absorb the reflected wave.

The velocity at the inlet boundary is determined by the inflow wind and wave condition. The top and bottom boundaries both adopt slip boundary conditions. In addition, the zero gradient condition is applied to the outlet boundary. Symmetrical condition is imposed on the sidewalls of the computational domain.

3.3 Wind and wave conditions

A uniform wind and a regular wave are chosen as inflow conditions for this study. Due to the large span of the turbine rotor along the tower height direction, the wind shear effect is considered using the wind profile power-law exponent [28] as:

$$U_z = U_{in}(z/H)^a \tag{9}$$

where z is the height, inflow wind speed U_{in} is set to 11.4m/s. The rotor speed and hub height are set as 12.1rpm and H=90m, respectively. a represents the wind shear index. A recommended value of 0.14 [29] for open sea condition is selected for the present simulations.

Stokes first-order deep-water wave is selected as the incident wave, with the wave period and wave height of 11.3s and 5.49m respectively. The wavelength (λ) is 199.3m.

3.4 Grid distribution

Different mesh resolutions are used in the computational domain, as shown in Figure 5. The region near the free surface has a relatively fine mesh with a grid size of 2m×2m×0.5m. To better capture the wake characteristics, the wake region also has a relatively high mesh resolution with size of 2m×2m×2m. The background mesh has a grid size of 8m×8m×8m, and the overall grid number in the CFD domain reaches 10.65 million.
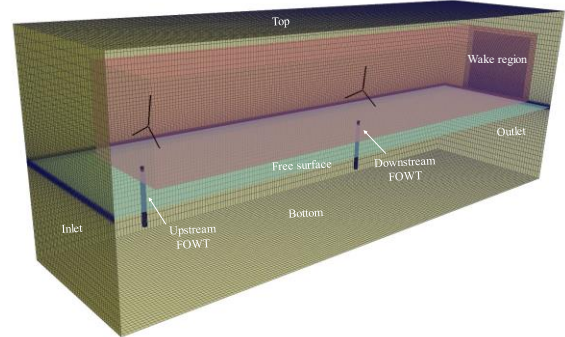

FIGURE 5: GRID DISTRIBUTION

Grid convergence test is conducted to determine the above grid numbers in the computation domain. Three sets of grids with different mesh resolutions are generated to perform mesh sensitivity analysis, which is summarized in Table 1. To reduce the computational time, platform motions of two tandem FOWTs

are fixed. In addition, the blade deformation is considered. A rated wind speed of 11.4m/s and rotational speed of 12.1rpm of wind turbine are adopted. Figure 6 presents the time history of aerodynamic load of two tandem wind turbines under different gird sizes. The differences between the time-mean aerodynamic coefficients of WT #1 and WT #2 for medium mesh and fine mesh are all less than 2%. The differences of aerodynamic coefficients for coarse mesh and fine mesh are larger than 5%. Moreover, the differences between time-mean blade-tip displacements obtained from medium and fine mesh are less than 1%, which is summarized in Table 2. To balance the computation accuracy and efficiency, medium mesh is chosen to conduct the following simulations.

TABLE 1: DIFFERENT MESH RESOLUTIONS

Mesh	Gird size in wake region	Total grid number
Coarse	$2\sqrt{2}m \times 2\sqrt{2}m \times 2\sqrt{2}m$	5.03 million
Medium	$2m \times 2m \times 2m$	10.65 million
Fine	$\sqrt{2}m \times \sqrt{2}m \times \sqrt{2}m$	17.86 million
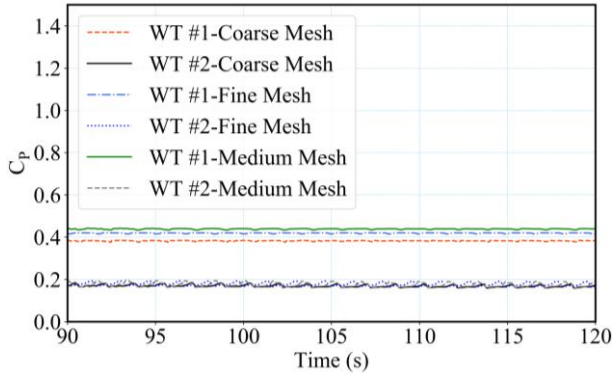
(a) AERODYNAMIC POWER COEFFICIENT
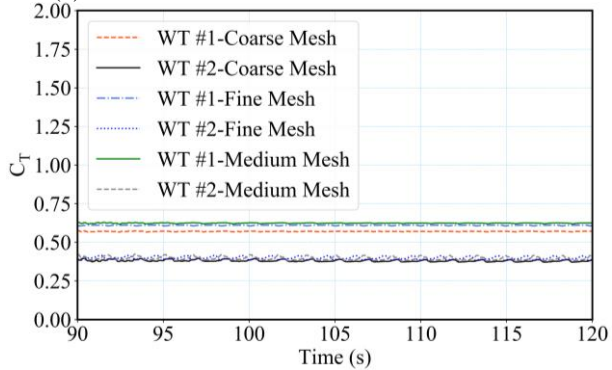
(b) AERODYNAMIC THRUST COEFFICIENT

**FIGURE 6:** TIME HISTORY OF AERODYNAMIC LOAD COEFFICIENTS UNDER DIFFERENT MESH RESOLUTIONS

TABLE 2: TIME-MEAN VALUES OF BLADE TIP-DISPLACEMENT UNDER DIFFERENT MESH RESOLUTIONS

| Mesh	WT #1			WT #2		
	δ_0(m)	δ_1(m)	δ_θ(deg)	δ_0(m)	δ_1(m)	δ_θ(deg)
Coarse	3.680	0.470	3.056	2.773	0.422	2.831
Medium	3.800	0.496	3.083	2.828	0.432	2.889
Fine	3.792	0.493	3.080	2.839	0.428	2.892

4. RESULTS AND DISCUSSION

In this section, the results will be presented starting with the spatial and time variation of blades deformations to illustrate their impacts on the wake interaction. The aerodynamic loading and the wake characteristics are then examined to highlight their influences on wind turbine aerodynamics. As a floating system, the discussions on the platform dynamics motions' responses induced by the blade deformation are also presented.
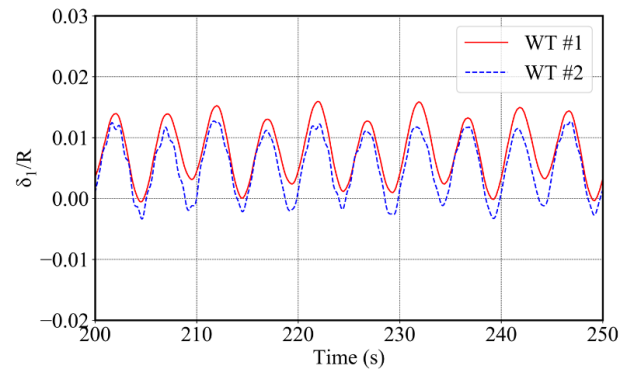
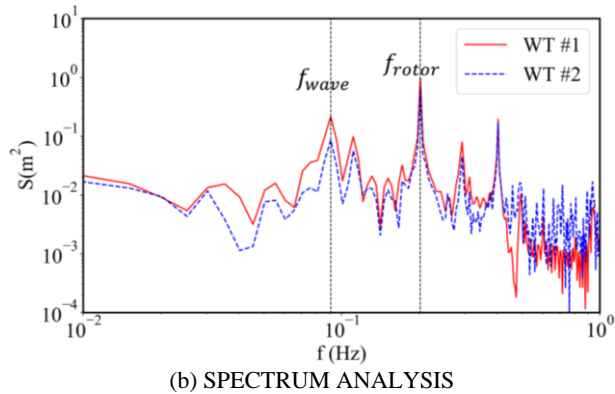### 4.1 Blade deformation
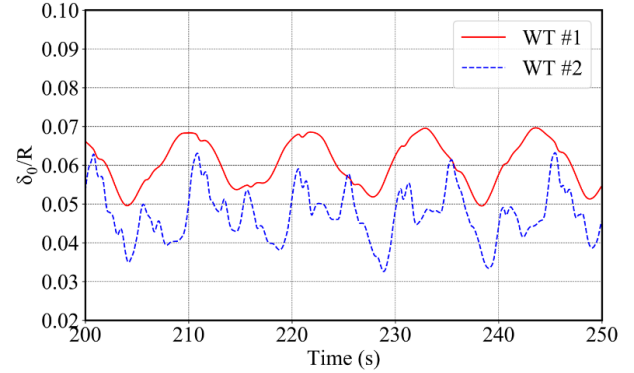
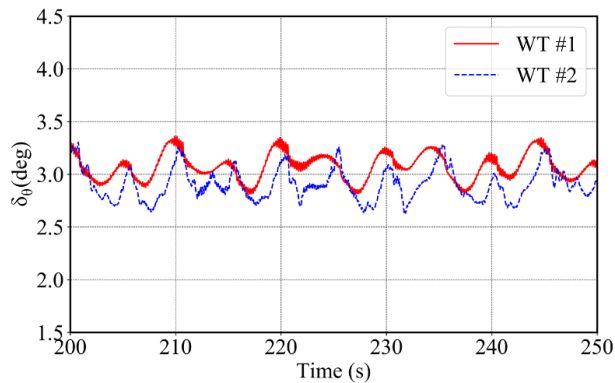(a) TIME HISTORY
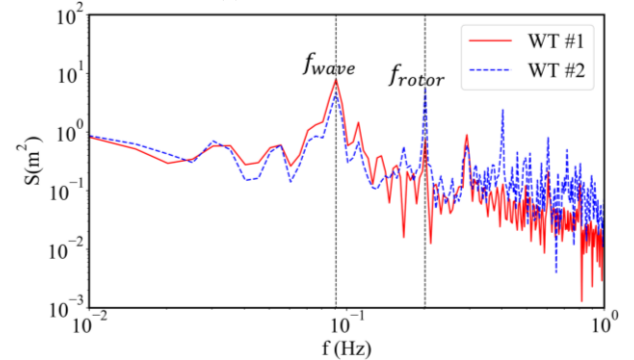
(b) SPECTRUM ANALYSIS

FIGURE 7: BLADE-TIP DISPLACEMENT ALONG FLAP-WISE DIRECTION (WT #1 AND WT #2 ARE UPSTREAM AND DOWNSTREAM FOWT, RESPECTIVELY)
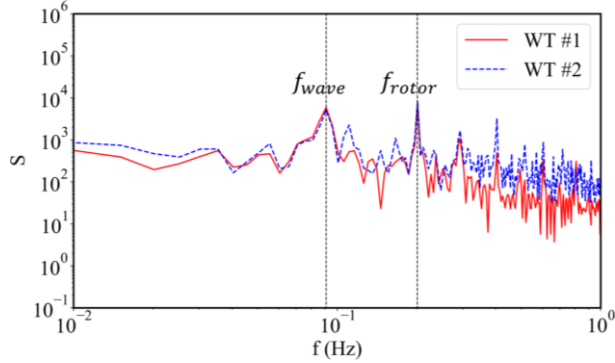

(a) TIME HISTORY

(b) SPECTRUM ANALYSIS

FIGURE 8: BLADE-TIP DISPLACEMENT ALONG EDGE-WISE DIRECTION
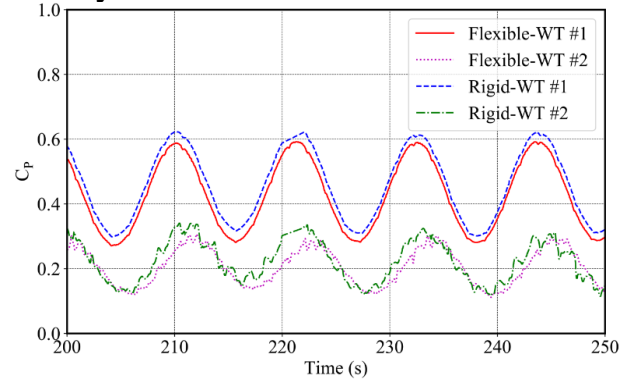

(a) TIME HISTORY

(b) FREQUENCY ANALYSIS

FIGURE 9: BLADE-TIP TORSIONAL DEFORMATION

Figures 7 and 8 show the time history and spectrum analysis of blade-tip displacement along flap-wise (δ_0), and edge-wise (δ_1) direction respectively. It can be seen that they both vary periodically with time, caused by the aerodynamic load and gravity force. For the upstream turbine (WT #1), both flap-wise and edge-wise displacements indicate there exist one dominant frequency (f_{wave} or f_{rotor}), which is consistent with the incident wave period and the turbine rotational speed respectively. However, the downstream turbine (WT #2) shows a wide frequency spectrum in addition to the above dominant frequency. This is more obvious with the flap-wise deformation in Figure 7, indicating that the wake influences more along flap-wise than in edge-wise direction. It can be attributed to the fact that bending along flap-wise is mainly controlled by aerodynamic forces, while bending along edgewise is dominated by gravity forces. Such differences can also be noted in the magnitude of δ_0 and δ_1. In fact, the time-mean value and variation amplitude for δ_0 of WT #2 are 0.83m smaller and 0.66m larger than those of WT #1, respectively. However, these differences of δ_1 decrease to 0.16m and 0.03m.

The blade torsional deformation (δ_θ) of WT #1 and WT #2 are presented in Figure 9. Different from the bending deformations, δ_θ has two dominant frequencies, i.e. the wave frequency (f_{wave}) and the rotational frequency (f_{rotor}), indicating that both aerodynamic and gravity forces are main causes of the torsional deformation. It is noted that the time-mean blade-tip torsional deformation can be as large as 3 degrees, this can significantly change the local AoA of the blades and further alter the aerodynamic performance, as will be discussed in Section 4.2.

4.2 Aerodynamic load

(a) AERODYNAMIC POWER COEFFICIENT
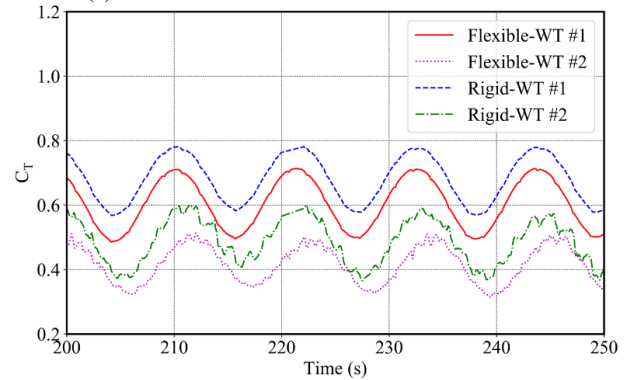
(b) AERODYNAMIC THRUST COEFFICIENT

FIGURE 10: TIME HISTORY OF AERODYNAMIC LOAD COEFFIEICENTS (FLEXIBLE MEANS BOTH WT #1 AND WT #2 CONSIDER BLADE DEFORMATION, WHILE RIGID MEANS BOTH WIND TURBINES DO NOT CONSIDER BLADE DEFORMATION)

Figure 10 shows time history of aerodynamic power coefficient (C_P) and aerodynamic thrust coefficient (C_T) of the two FOWTs with flexible and rigid blades. Both C_P and C_T periodically change with time regardless of the blade flexibility,

and this is believed to be the main reason leading to the periodic variation of δ_0 as discussed in Section 4.1. Compared with WT #1, WT #2 experiences lower inflow wind speed with higher turbulent intensity due to the turbine wake, resulting in the reduced time-mean aerodynamic coefficients and larger fluctuations.

To demonstrate how blades AoA are varied due to the deformation, Figure 11 displays the computed AoA contours in both time and spatial domain. As shown in Figure 11, α significantly decreases in the range of 0.5<r/R<1.0 (marked out with black circle) when the blade deformation is taking place. Refer to Eqs. (1)~(2), the deformation affects the aerodynamic performance by both altering the relative wind speed (U_{rel}) and changing the local AoA (α). Existing study reveals that the blade deformation induced velocity (U_S) is much smaller than inflow wind speed (U_{in}), therefore has little effect on the change of U_{rel} [30]. However, AoA is found to be significantly affected by the blade torsional deformation, thereby reduces the lift force and leads to smaller aerodynamic loading.


(a) UPSTREAM FOWT

(b) DOWNSTREAM FOWT
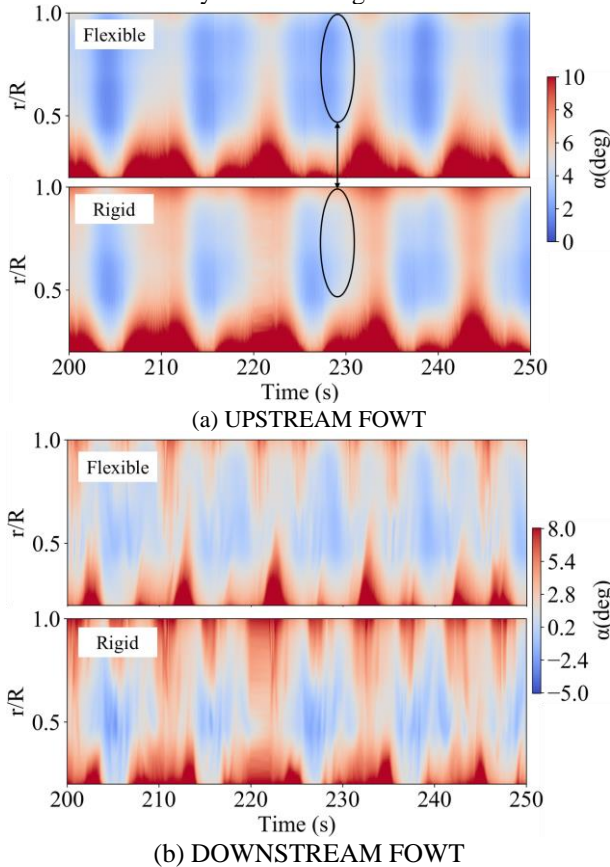
FIGURE 11: TEMPORAL AND SPATIAL DISTRIBUTION OF ANGLE OF ATTACK EXPERIENCED BY THE WIND TURBINE BLADE WITH AND WITHOUT STRUCTURAL DEFORMATION

In addition, it can also be observed that the α of WT #2 is much smaller than that of WT #1, which explains the reduced aerodynamic coefficients of WT #2 induced by the wake interaction. This is also consistent with the observations from C_P and C_T plotted in Figure 10. In addition, the decrease in the

amplitude of aerodynamic coefficients of WT #2, which is induced by the blade deformation, is found to be larger than that of WT #1.

4.3 Wake field

(a) WAKE VORTEX WITH BLADE DEFORMATION
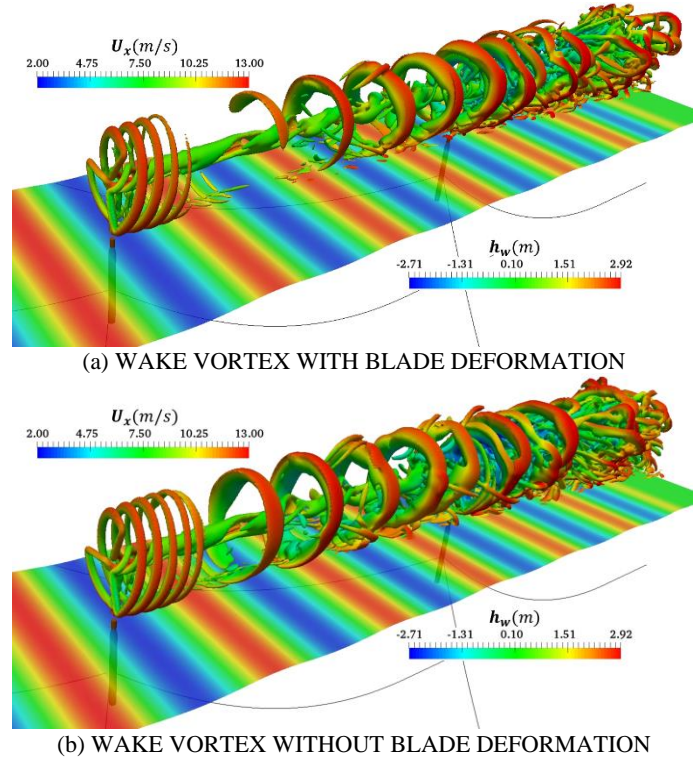
(b) WAKE VORTEX WITHOUT BLADE DEFORMATION
**FIGURE 12:** WAKE VOETEX STRUCTURE OF TWO TANDEM FOWTS WITH AND WITHOUT BLADE DEFORMATION
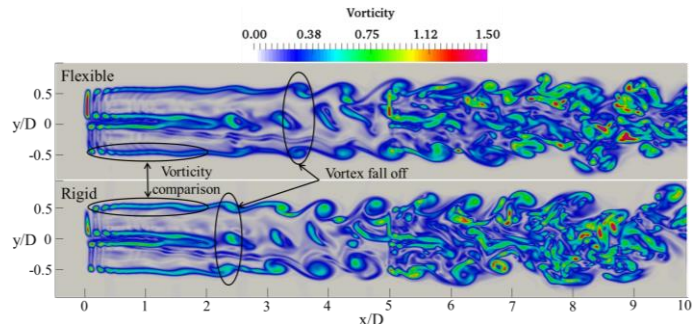
FIGURE 13: WAKE VORTICIY DISTRIBUTION IN THE HUB-HEIGHT PLANE

By altering the aerodynamic performance of FOWT, it is noted that the blade deformation also influences the wake characteristics. Figure 12 shows the instantaneous vortex structure in the wake field, which is visualized by Q=0.01 [31]. The wave surface and vortex structure are colored by the wave height (h_w) and axial flow speed (U_x) respectively. The spiral vortex structure generates and convects downstream in the wake of upstream turbine, the vortices gradually expand and merge into several large vortex rings. After the vortex rings pass through downstream turbine, they are broken down into small

vortices by the rotational blades. When the blade deformation is considered, the position where the spiral vortexes begin to merge into the vortex ring moves downwards as compared to that without deformation. This suggests that the wake vortexes from the rigid blades are more unstable and are much more easily rolled up and merged into the vortex ring, which can also be observed from the vorticity distribution at a horizontal plane with a hub height of z=90m as shown in Figure 13. Given the rigid blades, the vortex begins to fall off around 2D behind upstream turbine, while it increases to nearly 3D for flexible blades (indicated with circles). In addition, it can also be found that the magnitude of vorticity with flexible blades is slightly smaller than that with rigid blades (indicated with circles).

4.4 Platform motion

(a) SURGE MOTION

(b) PITCH MOTION
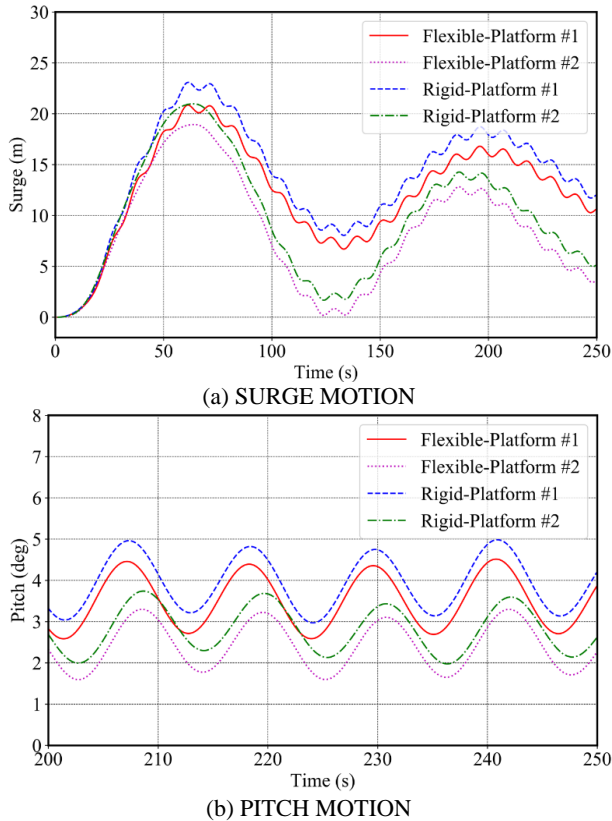
FIGURE 14: TIME HISTORY OF PLATFORM MOTIONS WITH AND WITHOUT BLADE DEFORMATION

Considering the interference effects between the wind turbine and the floating support platform, the variation of aerodynamic loads induced by the blade deformation changes the platform motion responses. As indicated in the previous study [12], the time-mean platform surge displacement and platform pitch angle mainly depend on the aerodynamic thrust of the wind turbine. Therefore, the decrease of aerodynamic forces, induced by the blade deformation, results in smaller platform motions as indicated in Figure 14 where the time history of platform motion responses for surge and pitch motions are displayed. For the upstream FOWT, time-mean surge

displacement and platform pitch angle decrease 11% and 12%, respectively, while for the downstream FOWT, the decrease in the amplitudes are both about 14%.

5. CONCLUSION

In this paper, an improved ALM and in-house CFD code based on OpenFOAM are employed to perform numerical simulations for two spar-type FOWTs with a tandem layout under given regular wave and uniform wind conditions. The wind turbine blades are replaced with virtual actuator lines to greatly reduce the computation amount. Euler-Bernoulli beam model and 1D FEM method are adopted to calculate the bending and torsional deformations of wind turbine blades. The 6DoF platform motions of FOWTs are taken into account. Coupled aero-hydro-elastic responses of the FOWT with rigid and flexible blades are compared to examine the influence of blade deformation on the wake interaction.

Our results show that the blade bending, and torsional deformation are both affected by the turbine wake interaction. As a result of that, the time-mean aerodynamic loading is reduced, while the fluctuation amplitude is increased. When the blade deformation is considered, the angle of attack experienced by the rotating blades is significantly decreased, further leading to the reduction of aerodynamic loads. Moreover, the aerodynamic thrust is more sensitive to the deformation than the aerodynamic power. In addition, the wake vortexes generated from the flexible blades are more stable compared with those from the rigid blades, and the magnitude of wake vorticity becomes smaller when the blade flexibility is included. The platform surge displacement and platform pitch angle also decrease with the decrease of aerodynamic loads, as induced by the blade deformation.

The present work contributes to the wake interactions of FOWTs with 6DoF motions. However, limited by the actuator line technique and 1D FEM method used in this study, the flow details around the blade surface and the shear deformation of wind turbine blades cannot be fully captured. Moreover, only uniform inflow and regular wave conditions are considered in this work. Better understandings on the blade deformation influence on the wake interaction of FOWTs can be achieved via further studies on the wind turbine layout arrangement and various atmospheric wind conditions in the future.

REFERENCES

[1] Irfan M, Hao Y, Panjwani M K, et al. Competitive assessment of South Asia's wind power industry: SWOT analysis and value chain combined model[J]. Energy Strategy Reviews, 2020, 32: 100540.

[2] Nilsson K, Ivanell S, Hansen K S, et al. Large‐eddy simulations of the Lillgrund wind farm[J]. Wind Energy, 2015, 18(3): 449-467.

[3] Troldborg N, Larsen G C, Madsen H A, et al. Numerical simulations of wake interaction between two wind turbines at various inflow conditions[J]. Wind Energy, 2011, 14(7): 859-876.

[4] Sørensen N N. General purpose flow solver applied to flow over hills[D]. 1995.

[5] Chanprasert W, Sharma R, Cater J E, et al. Large Eddy Simulation of Wind Turbine Fatigue Loading and Yaw Dynamics Induced by Wake Turbulence[J]. Available at SSRN 3955623, 2021.

[6] Churchfield M, Lee S, Moriarty P. Overview of the simulator for wind farm application (SOWFA)[J]. National Renewable Energy Laboratory, 2012.

[7] Rai R K, Gopalan H, Sitaraman J, et al. A code-independent generalized actuator line model for wind farm aerodynamics over simple and complex terrain[J]. Environmental modelling & software, 2017, 94: 172-185.

[8] Rezaeiha A, Micallef D. Wake interactions of two tandem floating offshore wind turbines: CFD analysis using actuator disc model[J]. Renewable Energy, 2021, 179: 859-876.

[9] Rezaeiha A, Micallef D. CFD simulation of two tandem floating offshore wind turbines in surge motion[C]//Journal of Physics: Conference Series. IOP Publishing, 2020, 1618(5): 052066.

[10] Huang Y, Wan D. Numerical Study on Aero-Hydrodynamics With Inter-Turbine Spacing Variation for Two Floating Offshore Wind Turbines[C]//International Conference on Offshore Mechanics and Arctic Engineering. American Society of Mechanical Engineers, 2019, 58899: V010T09A020.

[11] Huang Y, Cheng P, Wan D C. Numerical analysis on two floating offshore wind turbines with different layouts[C]//The 9th International Conference on Computational Methods. Rome, Italy. 2018.

[12] Cheng P, Huang Y, Wan D. A numerical model for fully coupled aero-hydrodynamic analysis of floating offshore wind turbine[J]. Ocean Engineering, 2019, 173: 183-196.

[13] Li P, Cheng P, Wan D C, et al. Numerical simulations of wake flows of floating offshore wind turbines by unsteady actuator line model[C]//Proceedings of the 9th international workshop on ship and marine hydrodynamics, Glasgow, UK. 2015: 26-28.

[14] Jonkman J M, Jonkman B J. FAST modularization framework for wind turbine simulation: full-system linearization[C]//Journal of Physics: Conference Series. IOP Publishing, 2016, 753(8): 082010.

[15] Bose B K. Global warming: Energy, environmental pollution, and the impact of power electronics[J]. IEEE Industrial Electronics Magazine, 2010, 4(1): 6-17.

[16] Bae Y H, Kim M H. Aero-elastic-control-floater-mooring coupled dynamic analysis of floating offshore wind turbine in maximum operation and survival conditions[J]. Journal of offshore mechanics and Arctic engineering, 2014, 136(2).

[17] Liu Y, Xiao Q, Incecik A, et al. Aeroelastic analysis of a floating offshore wind turbine in platform‐induced surge motion using a fully coupled CFD‐MBD method[J]. Wind Energy, 2019, 22(1): 1-20.

[18] Huang Y, Wan D, Hu C. Numerical Analysis of Aero-Hydrodynamic Responses of Floating Offshore Wind Turbine Considering Blade Deformation[C]//The 31st International Ocean and Polar Engineering Conference. OnePetro, 2021.

[19] Huang Y. Numerical investigation on coupled aero-hydro-elastic responses and wake interactions of floating wind turbines [D]. 2021.

[20] Chen G. Research on aeroelasticity and geometrical adaptiveness of large-scale wind turbine blades [D]. 2018.

[21] Sørensen J N, Shen W Z. Numerical modeling of wind turbine wakes[J]. Journal of Fluids Engineering, 2002, 124(2): 393-399.

[22] Dokainish M A, Subbaraj K. A survey of direct time-integration methods in computational structural dynamics—I. Explicit methods[J]. Computers & Structures, 1989, 32(6): 1371-1386.

[23] Adhikari S. Structural dynamic analysis with generalized damping models: analysis[M]. John Wiley & Sons, 2013.

[24] Pilkey D F. Computation of a damping matrix for finite element model updating[D]. Virginia Polytechnic Institute and State University, 1998.

[25] Liang Z, Lee G C. Representation of damping matrix[J]. Journal of Engineering Mechanics, 1991, 117(5): 1005-1019.

[26] Jonkman J, Musial W. Offshore code comparison collaboration (OC3) for IEA Wind Task 23 offshore wind technology and deployment[R]. National Renewable Energy Lab.(NREL), Golden, CO (United States), 2010.

[27] Jonkman J, Butterfield S, Musial W, et al. Definition of a 5-MW reference wind turbine for offshore system development[R]. National Renewable Energy Lab.(NREL), Golden, CO (United States), 2009.

[28] Irwin J S. A theoretical variation of the wind profile power-law exponent as a function of surface roughness and stability[J]. Atmospheric Environment (1967), 1979, 13(1): 191-194.

[29] Obhrai C, Kalvig S, Gudmestad O T. A review of current guidelines and research on wind modelling for the design of offshore wind turbines[C]//The Twenty-second International Offshore and Polar Engineering Conference. OnePetro, 2012.

[30] Huang Y, Wan D. Numerical analysis of aeroelastic responses of wind turbine under uniform inflow[C]//International Conference on Offshore Mechanics and Arctic Engineering. American Society of Mechanical Engineers, 2020, 84416: V009T09A041.

[31] Jeong J, Hussain F. On the identification of a vortex[J]. Journal of fluid mechanics, 1995, 285: 69-94.